CHEMISTRY

Covalent organic frameworks bearing Ni active sites for free radical-mediated photoelectrochemical organic transformations

Cheng Lin[1,2]†, Zhen Shan[1]†, Chaoran Dong[1], Yuan Lu[2], Weikun Meng[1], Gen Zhang[1]*, Bo Cai[3], Guanyong Su[1]*, Jong Hyeok Park[2]*, Kan Zhang[1]*

Photoelectrochemical (PEC) organic transformations occurring at anodes are a promising strategy for circumventing the sluggish kinetics of the oxygen evolution reaction. Here, we report a free radical-mediated reaction instead of direct hole transfer occurring at the solid/liquid interface for PEC oxidation of benzyl alcohol (BA) to benzaldehyde (BAD) with high selectivity. A bismuth vanadate ($BiVO_4$) photoanode coated with a 2,2′-bipyridine–based covalent organic framework bearing single Ni sites (Ni-TpBpy) was developed to drive the transformation. Experimental studies reveal that the reaction at the Ni-TpBpy/$BiVO_4$ photoanode followed first-order reaction kinetics, boosting the formation of surface-bound ·OH radicals, which suppressed further BAD oxidation and provided a nearly 100% selectivity and a rate of 80.63 μmol hour^{-1} for the BA-to-BAD conversion. Because alcohol-to-aldehyde conversions are involved in the valorizations of biomass and plastics, this work is expected to open distinct avenues for producing key intermediates of great value.

INTRODUCTION

Aqueous photoelectrochemical (PEC) cells have been investigated extensively for use in processes that use photons to break stable chemical bonds, which is an important approach to artificial photosynthesis (*1*–*5*). Nevertheless, in aqueous PEC cells, the photogenerated holes generally participate in the four-electron oxygen evolution reaction (OER), and the sluggish kinetics and generation of the inexpensive product O_2 seriously limit the overall PEC efficiency and "photon economy" of the process (*6*–*9*). Therefore, increasing effort has been devoted to circumventing this problem by using various alternative oxygenation reactions, and improved reaction kinetics and simultaneous formation of new chemical bonds are expected (*10*–*14*). A variety of PEC oxidations of organic molecules to more valuable molecules have been developed, including 5-hydroxymethylfurfural oxidation (*15*), glucose oxidation (*16*), and glycerol (GLY) oxidation (*17*), which show promise in valorizing biomass, plastics, and chemical intermediates. Note that the majority of the conversions of those organic molecules to other molecules involve alcohol and aldehyde oxidation to the corresponding acids, but the selective oxidation of alcohol to aldehyde faces a big challenge of easier aldehyde oxidation. Because aldehydes are generally key intermediates used in producing various chemicals, it is of great significance to realize highly selective conversions of alcohols to aldehydes.

In principle, PEC oxidations of organic substrates occur by directly capturing the photogenerated holes at the liquid/solid interface, which are oxygenated by H_2O or other oxygen atom donors. The mechanism is thought to be a hole-coupling oxygen atom transfer process (*18*–*20*), which could be a crucial reason behind the uncontrollable alcohol oxidations toward aldehydes. In most cases of electrochemical alcohol oxidations documented thus far, oxidation processes occur at Ni-based hydroxides or oxyhydroxides, and the Ni-based compound acts as a hydrogen-defective catalyst to dehydrogenate the alcohol for highly selective aldehyde production (*21*–*25*). It is reasonable to expect that selective conversions of alcohols to aldehydes in aqueous PEC cells would be those in which hole transfer is coupled with dehydrogenation at the PEC liquid/solid interface, which, however, remains to be explored.

In this work, we report a radical-mediated PEC organic transformation, which provides a highly selective conversion of benzyl alcohol (BA) to benzaldehyde (BAD). A 2,2′-bipyridine–based covalent organic framework bearing single Ni sites (Ni-TpBpy) was grown in situ on an amino-functionalized $BiVO_4$ photoanode (hereafter called Ni-TpBpy/$BiVO_4$), which enhanced the formation of adsorbed ·OH by the single surface-trapped hole. Transfer of the adsorbed ·OH instead of direct surface hole transfer for BA oxidation enabled an impressive BAD yield of 80.63 μmol hour^{-1} with a selectivity of near 100% at 1.23 V versus the reversible hydrogen electrode (V_{RHE}) within 4 hours and outperformed most previously reported processes. On the basis of comprehensive experimental measurements, a reaction mechanism for selective PEC oxidation of BA toward BAD over Ni-TpBpy/$BiVO_4$ was deduced.

RESULTS

Basic characterization of Ni-TpBpy/$BiVO_4$ photoanode

A porous $BiVO_4$ photoanode was prepared by a previously reported electrodeposition method (*26*), and Ni-TpBpy was synthesized via condensation of 1,3,5-triformylphloroglucinol (Tp) and 5,5′-diamino-2,2′-bipyridine (Bpy), followed by embedding Ni ions into the framework. N 1s x-ray photoelectron spectroscopy (XPS) showed that the peak for pyridinic N in the TpBpy spectrum was shifted to a higher binding energy after the introduction of the Ni

[1]Nanjing University of Science and Technology, Nanjing 210094, China. [2]Department of Chemical and Biomolecular Engineering, Yonsei University, 50 Yonsei-ro, Seodaemun-gu, Seoul 120-749, Republic of Korea. [3]Institute of Advanced Materials, Nanjing University of Posts and Telecommunications, Nanjing 210023, China.
*Corresponding author. Email: zhanggen@njust.edu.cn (G.Z.); sugy@njust.edu.cn (G.S.); lutts@yonsei.ac.kr (J.H.P.); zhangkan@njust.edu.cn (K.Z.)
†These authors contributed equally to this work.

ions, indicating that Ni was coordinated by the pyridinic N, which was consistent with previous reports (fig. S1) (*27*–*28*). The x-ray diffraction (XRD) peaks of pristine Ni-TpBpy were well matched with those in a simulated spectrum, and two obvious diffraction peaks at 3.7° and 27° were observed (fig. S2). The former originated from the long-range ordered structure and framework, while the latter was ascribed to π-π stacking interactions between adjacent layers (*29*–*30*). The pristine Ni-TpBpy presented a framework-like morphology with uniform distributions of C, N, O, Cl, and Ni elements (fig. S3). The ultraviolet-visible (UV-vis) absorption spectrum showed that pristine Ni-TpBpy had an absorption edge at 785 nm, resulting in a bandgap of 1.88 eV (fig. S4). To obtain Ni-TpBpy/$BiVO_4$ with an intimate interface, the $BiVO_4$ surface was first functionalized with amino groups by using 3-aminopropyltriethoxysilane (APTS) for in situ growth of the Ni-TpBpy (see the experimental details in the Supplementary Materials, fig. S5). Fourier transform infrared (FTIR) spectroscopy of the characteristic peaks for Ni-TpBpy and $BiVO_4$ emerge from the FTIR spectrum of the Ni-TpBpy/$BiVO_4$ photoanode (fig. S6). The XPS results showed increased amounts of chemisorbed oxygen species (O_C) and new peaks for C═O in the O 1s spectrum of Ni-TpBpy/$BiVO_4$ relative to that for pristine BiVO4 (fig. S7) (*31*), which indicated successful grafting of Ni-TpBpy onto the surface of $BiVO_4$. The Bi 4f and V 2p peaks exhibited slight shifts toward lower binding energies, whereas the Ni 2p peaks moved to higher binding energies, which were ascribed to the strong coupling at the interface between $BiVO_4$ and Ni-TpBpy. The morphology of the Ni-TpBpy/$BiVO_4$ photoanode was investigated with scanning electron microscopy (SEM) and transmission electron microscopy (TEM). As shown in fig. S8, the Ni-TpBpy/$BiVO_4$ photoanode displayed a morphology similar to that of the bare $BiVO_4$ photoanode, and no agglomeration of Ni-TpBpy or pore blocking on $BiVO_4$ was observed. The TEM image showed that an overlayer of Ni-TpBpy with a thickness of 10 nm was uniformly covered on the $BiVO_4$ surface, where a lattice spacing of 0.308 nm corresponds to the (121) plane of monoclinic phase $BiVO_4$. High-angle annular bright-field–scanning TEM (STEM)–energy-dispersive spectroscopy (EDS) images displayed uniform distributions of the Cl, N, Ni, O, Bi, and V elements (Fig. 1A). The band level alignment between Ni-TpBpy and $BiVO_4$ was established by UV photoelectron spectroscopy (UPS). As shown in Fig. 1 (B and C), the work functions of $BiVO_4$ and Ni-TpBpy were determined by subtracting the cutoff energies (E_{cutoff}) for the secondary electrons from the He I excitation energy (21.22 eV; left). The positions of the valence band (VB) maxima with respect to the Fermi levels were obtained from the onset of VB photoemission at the low–binding energy edges of the UPS spectra (right) (*32*). By combining Tauc plots (fig. S9) and the UPS spectra, the detailed band positions for $BiVO_4$ and Ni-TpBpy were acquired, as shown in Fig. 1D, which determined a type II heterojunction that favored hole transfer from $BiVO_4$ to the Ni-TpBpy overlayer. Because of the thin Ni-TpBpy overlayer, the Ni-TpBpy/$BiVO_4$ photoanode only exhibited the features of monoclinic $BiVO_4$ in the XRD pattern (fig. S10) and the $BiVO_4$ absorption edge in the UV-vis spectra. However, transient-state surface photovoltage (TS-SPV) measurements of the Ni-TpBpy/$BiVO_4$ photoanode demonstrated a markedly enhanced signal intensity with a longer-lived hole charge lifetime compared to the $BiVO_4$ photoanode, indicating that the band level alignment and the 10-nm Ni-TpBpy layer had a notable effect on boosting the charge separation (fig. S11). An electrochemical Nyquist plot for the Ni-TpBpy/$BiVO_4$ photoanode delivered smaller semicircular radiuses than that of the $BiVO_4$ photoanode, meaning a decreased resistance to charge transfer (fig. S12). Accordingly, the PEC behaviors of $BiVO_4$ and Ni-TpBpy/$BiVO_4$ were investigated in a 0.5 M K_3BO_3 (pH 9.1) electrolyte under AM 1.5 G illumination (100 mW cm^{-2}). Because of the enhanced charge separation efficiency, Ni-TpBpy/$BiVO_4$ achieved a photocurrent density of 3.84 mA cm^2 at 1.23 V_{RHE}, which was 2.4 times that of pristine $BiVO_4$ (1.57 mA cm^2) (Fig. 1E). In addition, the amino-functionalized method to integrate $BiVO_4$ with Ni-TpBpy is also applied to other metal oxide photoanodes (figs. S13 to S15).

Selective PEC BA oxidation to BAD

To evaluate the possibility of selective alcohol oxidation to the aldehyde over $BiVO_4$ and Ni-TpBpy/$BiVO_4$, the BA organic substrate was added to the 0.5 M K_3BO_3 electrolyte. Compared to those for water oxidation, the photocurrent densities of the $BiVO_4$ and Ni-TpBpy/$BiVO_4$ photoanodes were increased to 1.89 and 4.24 mA cm^2 at 1.23 V_{RHE} in the presence of BA, respectively, indicating that interfacial BA oxidation facilitates charge separation efficiency (Fig. 2A). The PEC BA oxidation products were investigated after irradiation for 4 hours at 1.23 V_{RHE}, as shown in fig. S16. The BA oxidation products formed at the $BiVO_4$ and Ni-TpBpy/$BiVO_4$ photoanodes were quantitatively analyzed with high-performance liquid chromatography (HPLC) (fig. S17), and the production rate and selectivity of oxidation products at various applied biases are shown in fig. S18. It can be seen that the BA peak at 4.5 min was almost absent for the Ni-TpBpy/$BiVO_4$ photoanode product; correspondingly, a BAD peak appeared at 5.4 min. The HPLC spectrum for BA oxidation over the $BiVO_4$ photoanode presented another peak at 3.2 min in addition to that for BAD, which corresponded to benzoic acid (BZA). These results demonstrated that BA was selectively converted to BAD over the Ni-TpBpy/$BiVO_4$ photoanode, while the $BiVO_4$ photoanode did not exhibit such high selectivity. Specifically, the BAD conversion ratio was only 12.3% with a selectivity of 71.2% after 4 hours over the $BiVO_4$ photoanode, whereas a markedly improved BAD conversion ratio of 81.4% and a selectivity of 99.1% were obtained with the Ni-TpBpy/$BiVO_4$ photoanode (Fig. 2B). The BAD conversion rate with the Ni-TpBpy/$BiVO_4$ system was maintained at a constant 80.63 μmol $hour^{-1}$ at 1.23 V_{RHE}, regardless of the BA concentration (Fig. 2C and fig. S19), which indicated that the BA-to-BAD conversion proceeded via first-order kinetics. During the reaction, the Faradaic efficiencies (FEs) of BZA with the bare $BiVO_4$ photoanode were increased while Ni-TpBpy/$BiVO_4$ photoanode can keep a nearly 100% FE for the BA-to-BAD conversion (fig. S20). Simultaneously, the generation of gas products may account for the discrepancy of total FEs with the $BiVO_4$ photoanode (fig. S21). In contrast, Ni-TpBpy/$BiVO_4$ can avoid the occurrence of competing OER. Crucially, the XPS spectra (fig. S22) and high-angle annular dark-field–STEM–EDS element maps (fig. S23) for the Ni-TpBpy/$BiVO_4$ photoanode did not show evident changes after PEC BA oxidation for 4 hours, revealing great photostability. Then, we further conducted the photostability test by Ni-TpBpy/$BiVO_4$ photoanode for a longer duration, as shown in fig. S24A, indicating a stable photocurrent density. Similar XRD patterns of Ni-TpBpy/$BiVO_4$ before and after measurement, along with slight dissolutions of V and Ni after testing, demonstrate a great photostability (fig. S24, B and C). The

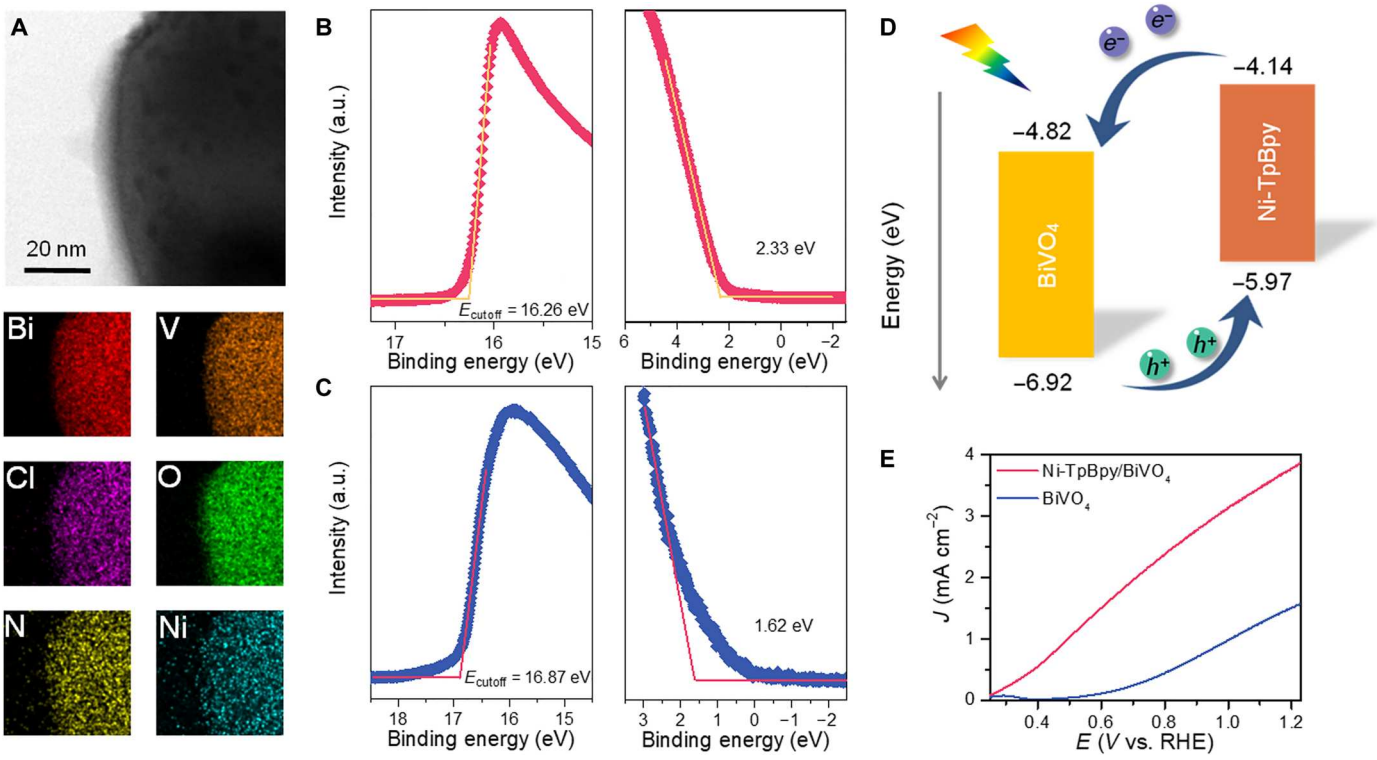

Fig. 1. Characterizations and PEC water oxidation performance of Ni-TpBpy/$BiVO_4$. (**A**) High-angle annular bright-field–STEM–EDS element maps for Ni-TpBpy/$BiVO_4$. Photoemission cutoff spectra (left) and VB position levels (right) for (**B**) $BiVO_4$ and (**C**) Ni-TpBpy. a.u., arbitrary units. (**D**) Schematic diagram of charge transport between $BiVO_4$ and Ni-TpBpy. (**E**) Linear sweep voltammogram (LSV) curves of the $BiVO_4$ and Ni-TpBpy/$BiVO_4$ photoanode.

conversion rate for the selective BA oxidation to BAD over the Ni-TpBpy/$BiVO_4$ photoanode outperforms most previously reported values acquired by others (Fig. 2D) (*33*–*40*).

There is no doubt that a higher photocurrent density contributes to greater BA conversion, based on which it is expected to clarify the BA oxidation process triggered by Ni-TpBpy/$BiVO_4$ photoanode from PEC performance, preliminarily. It is well known that the light absorbability and charge separation efficiency together with the surface reaction kinetics determine the PEC performance of a photoelectrode (*41*, *42*). Comparable photocurrent densities were calculated for the $BiVO_4$ and Ni-TpBpy/$BiVO_4$ photoanodes according to their light harvesting efficiencies (fig. S25). Then, we compared the carrier collection efficiencies by measuring the PEC efficiencies in the presence of 0.5 M sodium sulfate (Na_2SO_3), as shown in fig. S26. The charge transport efficiencies ($\eta_{transport}$) of the $BiVO_4$ and Ni-TpBpy/$BiVO_4$ photoanodes were evaluated with Eq. 3. As illustrated in Fig. 2E, the $BiVO_4$ photoanode exhibited a $\eta_{transport}$ value of 87.38% at 1.23 V_{RHE}, while the Ni-TpBpy/$BiVO_4$ photoanode revealed a slightly higher $\eta_{transport}$ of 92.36% at the same applied potential, which resulted from an appropriate band level alignment between the $BiVO_4$ and Ni-TpBpy. For the charge transfer efficiency ($\eta_{transfer}$) calculated with Eq. 4, a prominent improvement was observed for the Ni-TpBpy/$BiVO_4$ photoanode (73.99%) compared to the $BiVO_4$ photoanode (39.94%), proving that Ni-TpBpy played a vital role in surface hole transfer during the oxidation reaction (Fig. 2F). However, although the dark current of Ni-TpBpy/$BiVO_4$ showed a lower overpotential and higher current density relative to that of $BiVO_4$ (fig. S27), almost no BAD was produced via electrocatalysis at 1.23 V_{RHE} without illumination (fig. S28). These results implied that Ni-TpBpy did not act as a cocatalyst with high selectivity, in contrast to previously reported Ni-based hydroxide or oxyhydroxide electrocatalysts that facilitated alcohol oxidation by hydrogen defective effect. Therefore, the high selectivity for the BA-to-BAD conversion appeared to be mainly dependent on the photogenerated holes.

Important role of surface-bound ·OH radicals playing

To disclose the underlying mechanism, the rate for BA oxidation by the surface-trapped holes was established with light intensity variations in electrochemical impendence spectra (LI-EIS), as shown in fig. S29. The LI-EIS spectra were fitted with the equivalent model circuit (inset in fig. S12) and electrochemically active surface area (fig. S30), and the fitting results are shown in Fig. 3A and tables S1 and S2 (*43*, *44*). It can be seen that the reaction order of PEC BA oxidation over the pristine $BiVO_4$ is presumably 1.9, indicating a second-order reaction occurs, meaning that two-hole transfer is involved in BA oxidation (*18*, *45*, *46*). However, the reaction order for the Ni-TpBpy/$BiVO_4$ photoanode was 0.95, indicating first-order reaction kinetics, for which the reaction is dominated by a single surface-trapped hole (*47*, *48*). Furthermore, electron paramagnetic resonance (EPR) spectra were obtained under visible light illumination by using 5,5-dimethyl-1-pyrroline-N-oxide (DMPO) as a trapping agent. As shown in Fig. 3B, Ni-TpBpy/$BiVO_4$ displayed the typical quartet signal for the DMPO-·OH adduct produced in the 0.5 M K_3BO_3 electrolyte, evidencing that ·OH was generated as a result of a single hole-transfer

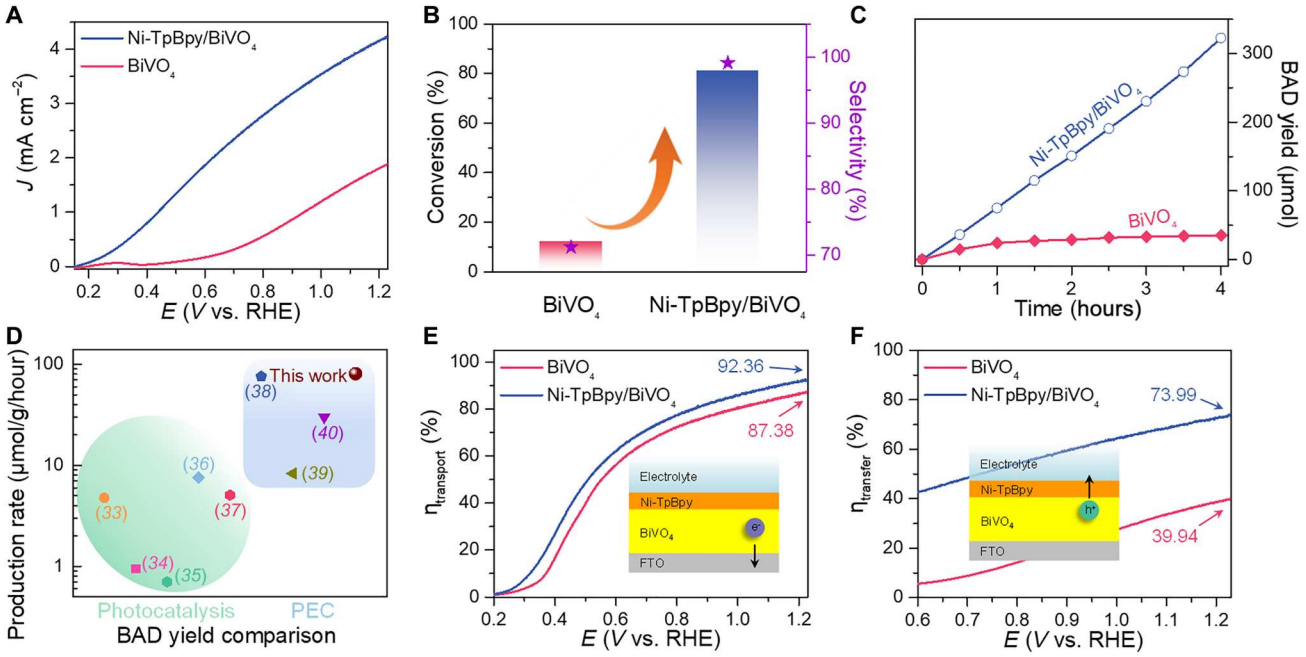

Fig. 2. PEC BA oxidation performances. (**A**) LSV curves for the $BiVO_4$ and Ni-TpBpy/$BiVO_4$ photoanodes measured in 0.5 M K_3BO_3 (pH 9.1) electrolyte containing 20 mM BA under AM 1.5 G illumination (100 mW cm^{-2}). BAD (**B**) conversion, selectivity, and (**C**) yield over $BiVO_4$ and Ni-TpBpy/$BiVO_4$ photoanodes after 4 hours of the PEC BA oxidation reaction. (**D**) Summary of BAD yields for BA oxidations. For ease of comparison, the units were converted to μmol g $hour^{-1}$. (**E**) Plots of $\eta_{transport}$ and (**F**) $\eta_{transfer}$ for $BiVO_4$ and Ni-TpBpy/$BiVO_4$ photoanodes measured in a 0.5 M K_3BO_3 (pH 9.1) electrolyte containing BA.

process. It is understandable that $BiVO_4$, which proceeded via a second-order reaction, showed almost no such signal. According to the UPS spectra (fig. S31A) and Tauc plot (fig. S4B), the band structure of Ni-TpBpy/$BiVO_4$ photoanode can meet the thermodynamic requirements of water oxidative OH radicals formation (fig. S31B).

To understand the effects of the ·OH radicals, we further carried out radical quenching experiments. As shown in Fig. 3C, when Na_2SO_3, was used as a hole scavenger, BAD production almost ceased, confirming the important role of the photogenerated holes in BA oxidation. The yield of BA was slightly increased when the electron scavenger $AgNO_3$ was added, which might have been due to the retardation of charge recombination. When potassium iodide (KI) was used as a quenching agent for the ·OH radicals, the yield of BAD was markedly reduced. In contrast, although superoxide anion radicals ($\cdot O_2^-$) and singlet oxygen ($^1O_2$) are trapped by benzoquinone (BQ) and furfuryl alcohol (FFA), the BAD conversion was not affected. On the basis of these results, it can be concluded that the ·OH radicals formed by single surface-trapped holes might have been involved in BA oxidation. However, it is worth noting that ·OH radicals are widely regarded as the strongest oxidants of organic molecules, and they often result in nonselective oxidations of organics into CO_2 and water instead of value-added organic chemicals (*49*), while adsorbed ·OH radicals with reduced oxidizing power can yield selective oxidation of organics (*10*, *50*, *51*). Hence, photoluminescence (PL) measurements were conducted while using coumarin as a fluorescence probe to identify the state of the ·OH radicals in solution (*52*, *53*). As shown in Fig. 3D, the PL signal at 502 nm showed negligible intensity after the reaction. On the contrary, for the free ·OH radicals produced by cleaving H_2O_2, an intense PL signal can be observed. These results implied that the ·OH radicals were mainly adsorbed on the surface of Ni-TpBpy/$BiVO_4$ rather than being released into the solution. We then added H_2O_2 into the reaction solution containing BA to confirm the oxidation ability of free ·OH radicals. Figure S32 revealed that the BA was easily overoxidized to BZA by the free ·OH, demonstrating that the high selectivity of the PEC BA-to-BAD conversion at the Ni-TpBpy/$BiVO_4$ photoanode originated from adsorbed ·OH radicals. Furthermore, six new EPR peaks assigned to carbon-centered radicals emerged after when BA was added to the electrolyte, and the intensities increased with continuous irradiation (fig. S33). PEC GLY oxidation reaction was also carried out to evidence the important role that adsorbed ·OH radicals played, demonstrating that the adsorbed ·OH radicals are also favorable for selective conversion of GLY to C_3 products (fig. S34).

Further analysis of oxidation mechanism

To further clarify the hole transfer process in the PEC BA-to-BAD conversion over the Ni-TpBpy/$BiVO_4$ photoanode, we performed an isotopic labeling study with 10% $H_2{}^{18}O$ used as the electrolyte. As shown in Fig. 4A, liquid chromatography–high-resolution mass spectrometry showed that BAD (^{18}O) products were produced, uncovering that O atoms were transferred from the water to the BAD. In addition, the PEC BA oxidation reaction was also carried out in an acidic medium, which reveals that the adsorbed ·OH species, which played a crucial role in selective BA conversion toward BAD, are originating from water dissociation (fig. S35). FTIR spectra were collected to explore the states of BA adsorbed on the surfaces of various photoanodes (Fig. 4B). Two characteristic bands for δ (O—H) and υ (C—O) located at 1207 and 1079 nm^{-1} for pure BA, respectively. On the surfaces of $BiVO_4$ and TpBpy/$BiVO_4$

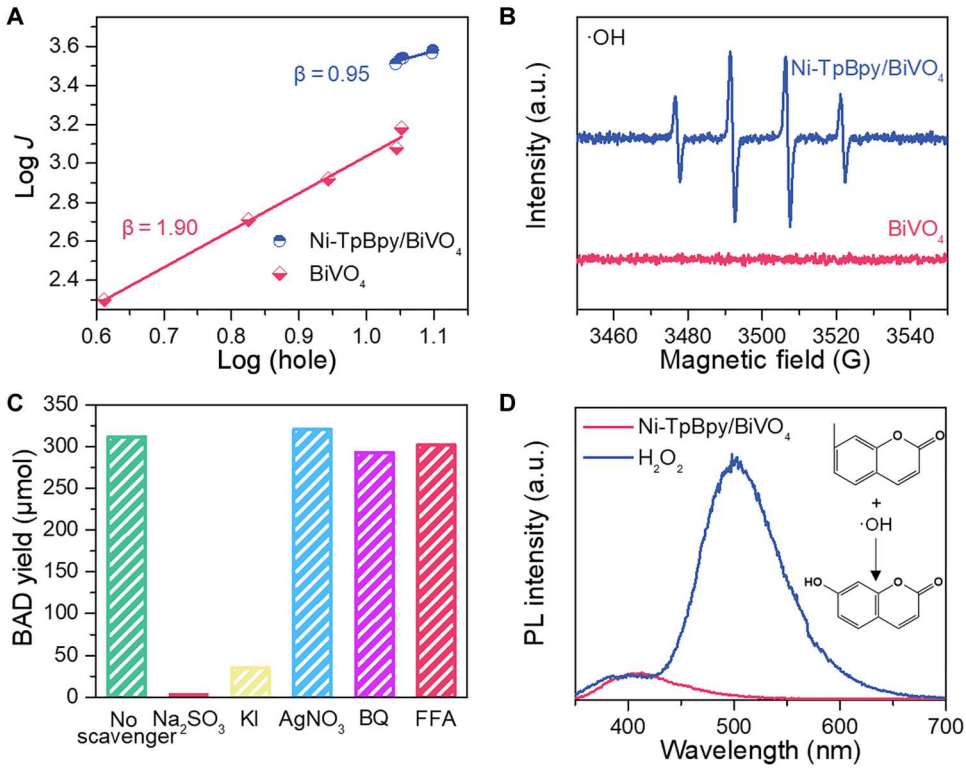

Fig. 3. The analysis of reaction kinetics and key radicals. (**A**) Relationship between the photocurrent (μA cm^{-2}) and surface hole density (number of holes nm^{-2}) for the $BiVO_4$ and Ni-TpBpy/$BiVO_4$ photoanodes in BA solution. (**B**) EPR spectra of the $BiVO_4$ and Ni-TpBpy/$BiVO_4$ photoanodes with DMPO used as a spin-trapping agent. (**C**) Yields of BAD at the Ni-TpBpy/$BiVO_4$ photoanode in the presence of various radical scavengers for 4 hours. (**D**) PL spectra for the ·OH radicals detected in the electrolyte after PEC BA oxidation reaction with coumarin used as a fluorescence probe. The measurements were performed in 0.5 M K_3BO_3 (pH 9.1) electrolyte.

photoanodes, all absorption bands of BA become weaker, which indicates that BA was not favorable for the adsorption on $BiVO_4$ and TpBpy/$BiVO_4$ photoanodes. In contrast, in addition to stronger peak intensities, the Ni-TpBpy/$BiVO_4$ photoanode revealed a negative shift of the C—O band and a weakened O—H band, which were consistent with the process that BA proceeded deprotonation was adsorbed onto the Ni-TpBpy via C—O bond (*54*). These observations suggested that the Ni ions anchored in TpBpy, as the active centers, enabled stronger BA adsorption, which was responsible for the higher BA conversion. Then, we turn our attention to figure out different BAD selectivities between $BiVO_4$ and Ni-TpBpy/$BiVO_4$ photoanodes. FTIR measurements were also performed to investigate BAD adsorption on the photoanodes, as shown in Fig. 4C. The bands at 1204 and 1695 cm^{-1} were assigned to the δ (C—H) and υ (C—O) bonds of BAD, respectively, of which the bands corresponding to C═O on the surfaces of $BiVO_4$ and Ni-TpBpy/$BiVO_4$ were shifted to lower frequencies, suggesting that BAD was adsorbed on the photoanodes through the C═O bond. Notably, weaker characteristic peaks were observed for the Ni-TpBpy/$BiVO_4$ photoanode than for the $BiVO_4$ photoanode. Therefore, we believe that the BAD produced from adsorbed BA is easily desorbed from the surface of Ni-TpBpy/$BiVO_4$ but not from the surface of $BiVO_4$, resulting in high selectivity without further oxidation of the BAD.

According to the above analysis, we propose a probable mechanism for selective PEC BA oxidation toward BAD on the Ni-TpBpy/$BiVO_4$ photoanode. The adsorption of BA initiates the first step for the oxidation half-reaction, during which BA underwent deprotonation and the Ni sites embedded in the TpBpy strengthen BA adsorption on the surface of the photoanode. Then, the adsorbed BA was converted to a carbon-centered radical and combined with the surface-bound ·OH radicals produced by water oxidation, which exhibited moderate oxidation capability. Given that the O atom of BAD was derived from H_2O, the C—O bond of BA was activated, and a proton was removed to produce BAD (Fig. 4D).

DISCUSSION

In this study, a radical-mediated reaction pathway induced by $BiVO_4$ coated with 2,2′-bipyridine–based COFs bearing single Ni sites was developed for selective oxidation of BA toward BAD. The decisive coating layer of Ni-TpBpy enabled the BAD conversion rate of the $BiVO_4$ photoanode to improve from 11.49 to 80.63 μmol $hour^{-1}$, whereas a selectivity of nearly 100% was obtained by the Ni-TpBpy/$BiVO_4$ photoanode. Comprehensive experimental measurements determined that surface-bound ·OH radicals produced by the Ni-TpBpy on $BiVO_4$ served as the main reactive oxygen species (ROS) responsible for the PEC BA oxidation reaction proceeding via first-order kinetics, avoiding subsequent overoxidation. The Ni sites embedded in TpBpy contributed to the enhanced adsorption of BA, and the Ni-TpBpy is conducive to the desorption of preferable BAD from the surface of the photoanode, resulting in a highly effective and selective PEC oxidation of

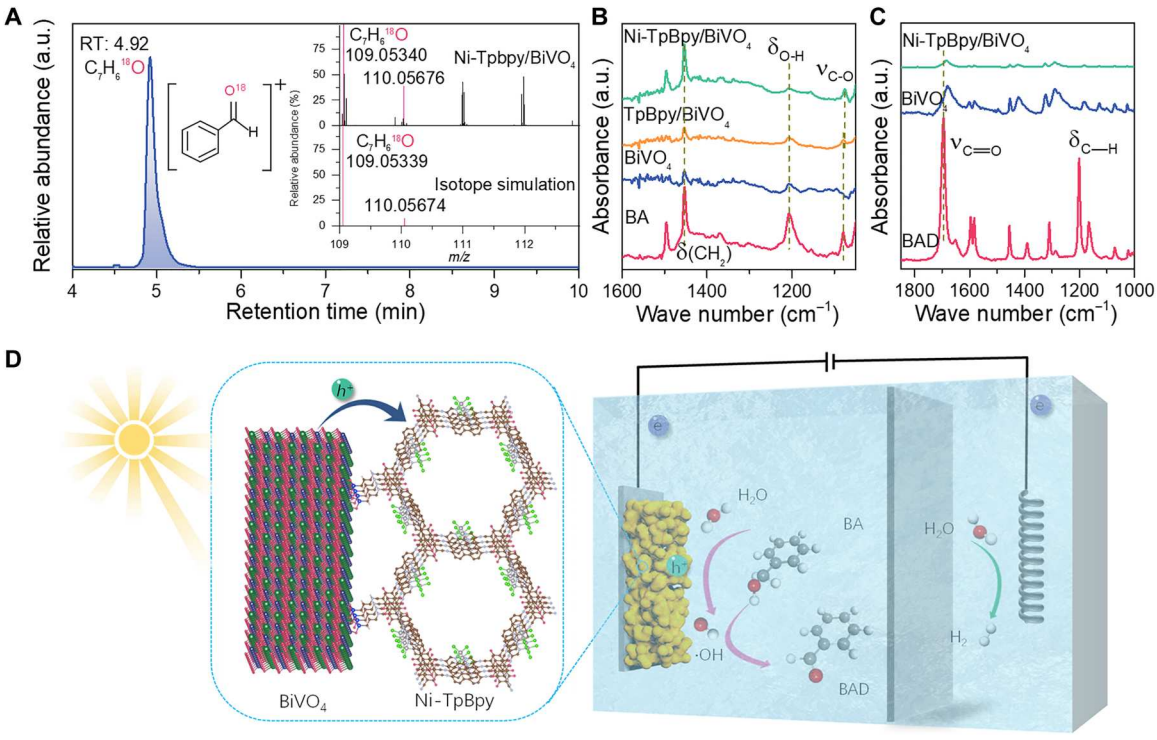

Fig. 4. The mechanism of selective PEC BA oxidation toward BAD. (**A**) Liquid chromatography–high-resolution mass spectrometry spectra for the BAD produced by PEC BA oxidation in an isotopically labeled electrolyte containing 20% $H_2{}^{18}O$. *m/z*, mass/charge ratio. RT, retention time. FTIR spectra of the different photoanodes after (**B**) BA and (**C**) BAD adsorption. (**D**) Mechanism proposed for selective BA activation by the Ni-TpBpy/$BiVO_4$ photoanode.

BA to BAD. This work is expected to provide a distinct strategy for producing crucial ROS required for biomass valorization.

MATERIALS AND METHODS

Preparation of $BiVO_4$ and other metal oxide photoanodes

The $BiVO_4$ photoanode was prepared on the basis of Kim and Choi's method (*26*). A 0.04 M $Bi(NO_3)_3$ solution was prepared by dissolving $Bi(NO_3)_3$•$5H_2O$ in 50 ml of a 0.4 M KI solution, and, then, its pH was adjusted to 1.7 by adding HNO_3. This solution was mixed with 20 ml of absolute ethanol (100%) containing 0.23 M *p*-BQ and was vigorously stirred for a few minutes. A typical three-electrode cell was used for electrodeposition. A fluorine-doped tin oxide (FTO) working electrode (WE), an Ag/AgCl (3 M KCl) reference electrode (RE), and a platinum counter electrode (CE) were used. A potentiostat (CH Instruments, CHI 660) was used for electrodeposition. The cathodic deposition was performed potentiostatically at −0.1 V versus Ag/AgCl for 5 min to obtain BiOI electrodes. Subsequently, 0.2 ml of a dimethyl sulfoxide solution containing 0.2 M vanadyl acetylacetonate [$VO(acac)_2$] was placed on the BiOI electrode and was heated in a muffle furnace at 450°C in the air to convert BiOI to $BiVO_4$. TiO_2, Fe_2O_3, and WO_3 photoanodes were prepared on the basis of previous reports (*18*, *48*, *55*).

Synthesis of TpBpy

TpBpy was prepared according to the literature methods with a little modification (*30*). A Pyrex tube was charged with triformylphloroglucinol (21 mg, 0.10 mmol) and 5,5′-diamino-2,2′-bipyridine (27.9 mg, 0.15 mmol) in 4.0 ml of a 3:1 v:v solution of *N*,*N*-dimethyl acetamide (DMAC):*o*-dichlorobenzene (*o*-DCB) with 0.2 ml of 6 M aqueous acetic acid as catalyst. This mixture was sonicated for 5 min to get a homogeneous dispersion. The tube was flash frozen at 77 K, evacuated, and flame-sealed. The reaction mixture was heated at 100°C for 3 days to afford an orange-red precipitate. The precipitate was isolated by filtration, wished by acetone, and dried under vacuum at 60°C overnight to afford TpBpy.

Synthesis of Ni-TpBpy

TpBpy (50 mg) was treated with $NiCl_2$·$6H_2O$ (30 mg) in the mixed solvent of 10 ml of CH_3OH and 10 ml of H_2O. The solution was stirred for 8 hours at 60°C. The solid was filtered washed with CH_3OH and H_2O and dried in a vacuum at 60°C overnight to give Ni-TpBpy.

Preparation of Ni-TpBpy/$BiVO_4$ and other Ni-TpBpy/metal oxide photoanodes

The $BiVO_4$ modified FTO glass was placed in a high-pressure reactor containing 30 ml of anhydrous toluene and 100 μl of APTS and kept at 100°C for 8 hours. After cooling to room temperature, the substrate was washed with toluene and dried at 100°C for later use. The abovementioned substrate was placed in a 20-ml glass bottle containing 10 mg of triformylphloroglucinol and 10 ml of *o*-DCB, followed by a reaction at 100°C for 8 hours. Then, the substrate was cooled to room temperature, and the excess monomer was washed away. Then, the substrate was transferred to a high-pressure reactor with triformylphloroglucinol (21 mg, 0.10 mmol) and 5,5′-diamino-2,2′-bipyridine (27.9 mg, 0.15 mmol) in 36 ml of a 3:1 v:v solution of DMAC:*o*-DCB with 0.6 ml of 6 M aqueous acetic acid

as catalyst. The reaction mixture was heated at 100°C for 3 days to afford TpBpy/$BiVO_4$ photoanode. Then, the film was treated with $NiCl_2{\cdot}6H_2O$ (30 mg) in the mixed solvent of 10 ml of CH_3OH and 10 ml of H_2O. The solution was stirred for 8 hours at 60°C, followed by washing with CH_3OH and H_2O, and dried in a vacuum at 60°C overnight to give Ni-TpBpy/$BiVO_4$. The preparations of other Ni-TpBpy/metal oxide photoanodes were the same as that of the Ni-TpBpy/$BiVO_4$ photoanode.

Characterizations

SEM images were obtained on a FEI Quant 250FEG. TEM characterizations were obtained on a Tecnai G2 F30 S-TWIN instrument with an EDS analyzer operated at an accelerating voltage of 300 kV. XRD patterns were measured on a Bruker D8 multipurpose XRD system. XPS spectra were obtained on a PHI QUANTERA II XPS. The reflectance and transmittance spectra were recorded by using UV-vis spectrophotometers (Shimadzu UV-3600). UPS was performed by PHI 5000 VersaProbe III with He I source (21.22 eV) under an applied negative bias of 9.0 V. FTIR spectra of BA and BAD adsorption were recorded using a Thermo Fisher Scientific (NICOLETIS10) spectrometer equipped with a KBr window. TS-SPV response measurements were used by a system equipped with a third-harmonic Nd:YAG laser (Polaris II, New Wave Research Inc.) and a 500-MHz digital phosphor oscilloscope (TDS 5054, Tektronix). Inductively coupled plasma optical emission spectrometry was carried out on an Agilent 720ES instrument. PL spectra were taken on Edinburgh FLS1000 equipped with an Oxford cryostat designed for optical measurement. The amount of gas was analyzed with a gas chromatograph (PerkinElmer Clarus 590). Room-temperature EPR measurements were carried out on a Bruker (a320) spectrometer (298 K, 9063.386 MHz). K_3BO_3 electrolyte (0.5 M) containing DMPO with a concentration of 10 mM was used for detection of ·OH radicals (without BA) and carbon-centered radicals (with BA), and the photoanode (0.1 cm by 0.1 cm) was placed into a reactor under Xe lamp irradiation with a 420-nm cutoff. The reaction solution was pumped into a paramagnetic tube.

PEC measurements

PEC measurements were conducted on an electrochemical workstation (CHI 760E) in a sealed H-type glass cell. Nafion 212 proton exchange membrane was used to separate the anode from the cathode chamber. The simulated solar illumination was obtained from a 300-W Xenon lamp (Beijing PerfectLight. Co. Ltd.) with an AM 1.5 G filter (100 mW cm^{-2}). The photoanodes were front-illuminated and used as the WE, while Ag/AgCl electrode and Pt sheet were used as the RE and CE, respectively. The electrolyte (20 ml) contains 0.5 M potassium borate buffer (K_3BO_3), prepared by adjusting the pH of 0.5 M H_3BO_3 solution to 9.1 with KOH at 25° C. In addition, The electrolyte contains 0.5 M Na_2SO_4 aqueous solution with pH adjusted to two 0.5 M H_2SO_4 solution. Before the PEC measurements, the electrolyte was purged with N_2 to remove dissolved oxygen. The photocurrent was recorded at a scan rate of 10 mV s^{-1} with and without the presence of 20 mM BA. The conversion between the potentials versus Ag/AgCl and the potentials versus RHE was performed using the following equation

$$E(\text{vs.RHE}) = E(\text{vs.Ag/AgCl}) + E_{\text{Ag/AgCl}} + 0.0591 \times \text{pH} \quad (1)$$

During the test of charge transport efficiency ($\eta_{transport}$) and charge transfer efficiency ($\eta_{transfer}$), we used Na_2SO_3 electrolyte as the hole scavenger. Here, $\eta_{transport}$ represents the proportion of the electrode/electrolyte interface photogenerated holes, while $\eta_{transfer}$ represents the proportion of those holes at the photoanode/electrolyte interface for BA oxidation

$$\eta_{\text{transport}} = \frac{J_{\text{Na}_2\text{SO}_3}}{J_{\text{abs}}} \quad (2)$$

$$\eta_{\text{transfer}} = \frac{J_{\text{BA}}}{J_{\text{Na}_2\text{SO}_3}} \quad (3)$$

where J_{BA} and $J_{Na_2SO_3}$ represent the photocurrent density tested in 0.5 M K_3BO_3 containing BA and Na_2SO_3, respectively. J_{abs} represents the unity converted photocurrent density that is achievable.

The single photon energy is calculated from Eq. 4

$$E(\lambda) = h \times C/\lambda \quad (4)$$

where $E(\lambda)$ is the photon energy (J), h is Planck's constant (6.626×10^{-34} Js), C is the speed of light (3×10^8 m s^{-1}), and λ is the photon wavelength (nanometers).

The solar photon flux is then calculated according to Eq. 5

$$\text{Flux}(\lambda) = P(\lambda)/E(\lambda) \quad (5)$$

where Flux(λ) is the solar photon flux (m^{-2} s^{-1} nm^{-1}) and $P(\lambda)$ is the solar power flux (W m^{-2} nm^{-1}). The theoretical absorbed photocurrent density under solar illumination (AM 1.5 G), J_{abs} (A m^{-2}), is then calculated by integrating the solar photon flux between 300 and 520 nm, shown in Eq. 6

$$J_{\text{abs}} = e \times \int_{300}^{520} \eta_{\text{harvest}} \text{Flux}(\lambda) d\lambda \quad (6)$$

where e is the elementary charge (1.602×10^{-19} C). The theoretical absorbed photocurrent densities of $BiVO_4$ and Ni-TpBpy/$BiVO_4$ photoanodes are accordingly calculated to be 5.75 and 6.02 mA cm^{-2} based on our solar spectra.

EIS and cyclic voltammogram spectra were conducted in 0.5 M K_3BO_3 containing BA.

PEC BA oxidation reaction was performed at room temperature by holding the illuminated photoanode at 1.23 V_{RHE} for 4 hours. The gas product at the anodic side was quantified by a gas chromatograph (PerkinElmer Clarus 590) equipped with a TCD detector. To quantitatively analyze the oxidation products, 50 μl of the solution was taken out from the cell and analyzed to calculate the yield of BAD using HPLC.

The conversion rate of BAD was calculated according to

$$\text{Conversion rate (BAD)} = \frac{C_{\text{BAD}} \times V}{t} \quad (7)$$

where V is the volume of the reaction solution and t is the reaction time.

The conversion ratio of BA and selectivity of BAD from BA were calculated on the basis of

$$\text{Conversion (BA)} = \frac{C_0 - C_r}{C_0} \times 100\% \quad (8)$$

$$\text{Selectivity (BAD)} = \frac{C_p}{C_0 - C_r} \times 100\% \quad (9)$$

where C_0 is the primary concentration of BA and C_r and C_p are the concentrations of left BA and BAD after a certain reaction time, respectively.

FEs of liquid products (LP) were calculated by

$$\begin{aligned}\text{FE (LP)} &= \frac{\text{Number of holes to oxidize BA to LP}}{\text{Number of all collected photogenerated holes}} \times 100\% \\ &= \frac{e_{LP} \times n_{LP} \times N}{Q/n} \times 100\% \\ &= \frac{e_{LP} \times c_{LP} \times V \times N}{Q/n} \times 100\% \end{aligned} \quad (10)$$

where e_{LP} is the number of holes required to oxidize one BA molecule to one LP molecule (2 for BAD and 4 for BZA), n_{LP} is the yield of LP determined by HPLC, N is Avogadro's constant, Q is the quantity of electric charge, and n is the elementary charge.

FE of O_2 was calculated on the basis of the following equation

$$\begin{aligned}\text{FE (O}_2\text{)} &= \frac{\text{Number of holes to oxidize H}_2\text{O to O}_2}{\text{Number of collected photogenerated holes}} \times 100\% \\ &= \frac{e_{o_2} \times n_{o_2} \times N}{Q/n} = \frac{4 \times n_{o_2} \times N}{Q/n} \end{aligned} \quad (11)$$

where e_{o_2} is the number of holes required to oxidize one H_2O molecule to one O_2 molecule and n_{o_2} is the yield of O_2 determined by gas chromatography.

To explore the major active species involved in the oxidation of BA, Na_2SO_3 was used as a hole scavenger, KI was used as an ·OH scavenger, $AgNO_3$ was used as an electron scavenger, 1,4-BQ used as an $\cdot O_2^-$ scavenger, and FFA used as an $^1O_2$ scavenger were added into PEC oxidation system.

Isotope-labeled H_2O was used to determine whether the hydroxyl radicals generated from water participated in the oxidation of BA. Except for the replacement of partial aqueous K_3BO_3 electrolyte by $H_2{}^{18}O$ ($VH_2{}^{18}O/V_{total} = 0.2$), the $H_2{}^{18}O$-labeling experiments were conducted under the same conditions as those used for PEC oxidation of BA. The identification of the oxidation products was performed using a liquid chromatograph coupled to a hybrid quadrupole Orbitrap high-resolution mass spectrometer (Thermo Fisher Scientific Inc., Waltham, MA) operated in positive atmospheric pressure chemical ionization mode. Chromatographic separations were performed on a Hypersil GOLD C18 column (100 mm by 2.1 mm by 1.9 μm; Thermo Fisher Scientific Inc.).

Supplementary Materials

This PDF file includes:

Fig. S1 to S35

Tables S1 and S2

REFERENCES AND NOTES

1. V. Andrei, G. M. Ucoski, C. Pornrungroj, C. Uswachoke, Q. Wang, D. S. Achilleos, H. Kasap, K. P. Sokol, R. A. Jagt, H. Lu, T. Lawson, A. Wagner, S. D. Pike, D. S. Wright, R. L. Z. Hoye, J. L. MacManus-Driscoll, H. J. Joyce, R. H. Friend, E. Reisner, Floating perovskite-$BiVO_4$ devices for scalable solar fuel production. *Nature* **608**, 518–522 (2022).
2. V. Andrei, R. A. Jagt, M. Rahaman, L. Lari, V. K. Lazarov, J. L. MacManus-Driscoll, R. L. Z. Hoye, E. Reisner, Long-term solar water and CO_2 splitting with photoelectrochemical BiOI-$BiVO_4$ tandems. *Nat. Mater.* **21**, 864–868 (2022).
3. Z. Wang, Y. Hu, S. Zhang, Y. Sun, Artificial photosynthesis systems for solar energy conversion and storage: Platforms and their realities. *Chem. Soc. Rev.* **51**, 6704–6737 (2022).
4. Y. Xiao, Z. Fan, M. Nakabayashi, Q. Li, L. Zhou, Q. Wang, C. Li, N. Shibata, K. Domen, Y. Li, Decoupling light absorption and carrier transport via heterogeneous doping in Ta_3N_5 thin film photoanode. *Nat. Commun.* **13**, 7769 (2022).
5. C. Dong, Y. Yang, X. Hu, Y. Cho, G. Jang, Y. Ao, L. Wang, J. Shen, J. H. Park, K. Zhang, Self-cycled photo-Fenton-like system based on an artificial leaf with a solar-to-H_2O_2 conversion efficiency of 1.46. *Nat. Commun.* **13**, 4982 (2022).
6. K. Zhang, J. Liu, L. Wang, B. Jin, X. Yang, S. Zhang, J. H. Park, Near-complete suppression of oxygen evolution for photoelectrochemical H_2O oxidative H_2O_2 synthesis. *J. Am. Chem. Soc.* **142**, 8641–8648 (2020).
7. Z. Zhang, X. Huang, B. Zhang, Y. Bi, High-performance and stable BiVO4photoanodes for solar water splittingviaphosphorus–oxygen bonded FeNi catalysts. *Energ. Environ. Sci.* **15**, 2867–2873 (2022).
8. B. Zhang, S. Yu, Y. Dai, X. Huang, L. Chou, G. Lu, G. Dong, Y. Bi, Nitrogen-incorporation activates $NiFeO_x$ catalysts for efficiently boosting oxygen evolution activity and stability of $BiVO_4$ photoanodes. *Nat. Commun.* **12**, 6969 (2021).
9. B. Zhang, X. Huang, Y. Zhang, G. Lu, L. Chou, Y. Bi, Unveiling the activity and stability origin of $BiVO_4$ photoanodes with FeNi oxyhydroxides for oxygen evolution. *Angew. Chem. Int. Ed. Engl.* **59**, 18990–18995 (2020).
10. J. Ma, K. Mao, J. Low, Z. Wang, D. Xi, W. Zhang, H. Ju, Z. Qi, R. Long, X. Wu, L. Song, Y. Xiong, Efficient photoelectrochemical conversion of methane into ethylene glycol by WO_3 nanobar arrays. *Angew. Chem. Int. Ed. Engl.* **60**, 9357–9361 (2021).
11. S. Huang, F. Feng, R.-T. Huang, T. Ouyang, J. Liu, Z.-Q. Liu, Activating C–H bonds by tuning Fe sites and an interfacial effect for enhanced methanol oxidation. *Adv. Mater.* **34**, e2208438 (2022).
12. Y. Song, Y. Wu, S. Cao, Y. Zhang, D. Luo, J. Gao, Z. Li, L. Sun, J. Hou, Simultaneous photoelectrocatalytic oxidation and nitrite-ammonia conversion with artificial photoelectrochemistry cells. *Adv. Energy Mater.* **12**, 2201782 (2022).
13. L. Luo, W. Chen, S. M. Xu, J. Yang, M. Li, H. Zhou, M. Xu, M. Shao, X. Kong, Z. Li, H. Duan, Selective photoelectrocatalytic glycerol oxidation to dihydroxyacetone via enhanced middle hydroxyl adsorption over a Bi_2O_3-incorporated catalyst. *J. Am. Chem. Soc.* **144**, 7720–7730 (2022).
14. Z. Li, L. Luo, M. Li, W. Chen, Y. Liu, J. Yang, S. M. Xu, H. Zhou, L. Ma, M. Xu, X. Kong, H. Duan, Photoelectrocatalytic C–H halogenation over an oxygen vacancy-rich TiO_2 photoanode. *Nat. Commun.* **12**, 6698 (2021).
15. H. G. Cha, K. S. Choi, Combined biomass valorization and hydrogen production in a photoelectrochemical cell. *Nat. Chem.* **7**, 328–333 (2015).
16. Z. Tian, Y. Da, M. Wang, X. Dou, X. Cui, J. Chen, R. Jiang, S. Xi, B. Cui, Y. Luo, H. Yang, Y. Long, Y. Xiao, W. Chen, Selective photoelectrochemical oxidation of glucose to glucaric acid by single atom Pt decorated defective TiO_2. *Nat. Commun.* **14**, 142 (2023).
17. D. Liu, J. C. Liu, W. Cai, J. Ma, H. B. Yang, H. Xiao, J. Li, Y. Xiong, Y. Huang, B. Liu, Selective photoelectrochemical oxidation of glycerol to high value-added dihydroxyacetone. *Nat. Commun.* **10**, 1779 (2019).
18. Y. Zhao, C. Deng, D. Tang, L. Ding, Y. Zhang, H. Sheng, H. Ji, W. Song, W. Ma, C. Chen, J. Zhao, α-Fe_2O_3 as a versatile and efficient oxygen atom transfer catalyst in combination with H_2O as the oxygen source. *Nat. Catal.* **4**, 684–691 (2021).
19. T. Li, T. Kasahara, J. He, K. E. Dettelbach, G. M. Sammis, C. P. Berlinguette, Photoelectrochemical oxidation of organic substrates in organic media. *Nat. Commun.* **8**, 390 (2017).
20. H. Tateno, S. Iguchi, Y. Miseki, K. Sayama, Photo-electrochemical C–H bond activation of cyclohexane using a WO_3 photoanode and visible light. *Angew. Chem. Int. Ed. Engl.* **57**, 11238–11241 (2018).
21. X. Han, H. Sheng, C. Yu, T. W. Walker, G. W. Huber, J. Qiu, S. Jin, Electrocatalytic oxidation of glycerol to formic acid by $CuCo_2O_4$ spinel oxide nanostructure catalysts. *ACS Catal.* **10**, 6741–6752 (2020).
22. B. J. Taitt, D.-H. Nam, K.-S. Choi, A comparative study of nickel, cobalt, and iron oxyhydroxide anodes for the electrochemical oxidation of 5-hydroxymethylfurfural to 2,5-furandicarboxylic acid. *ACS Catal.* **9**, 660–670 (2018).
23. M. T. Bender, Y. C. Lam, S. Hammes-Schiffer, K. S. Choi, Unraveling two pathways for electrochemical alcohol and aldehyde oxidation on NiOOH. *J. Am. Chem. Soc.* **142**, 21538–21547 (2020).

24. N. Zhang, Y. Zou, L. Tao, W. Chen, L. Zhou, Z. Liu, B. Zhou, G. Huang, H. Lin, S. Wang, Electrochemical oxidation of 5-hydroxymethylfurfural on nickel nitride/carbon nanosheets: Reaction pathway determined by in situ sum frequency generation vibrational spectroscopy. *Angew. Chem. Int. Ed. Engl.* **131**, 16042–16050 (2019).
25. T. Wang, L. Tao, X. Zhu, C. Chen, W. Chen, S. Du, Y. Zhou, B. Zhou, D. Wang, C. Xie, P. Long, W. Li, Y. Wang, R. Chen, Y. Zou, X.-Z. Fu, Y. Li, X. Duan, S. Wang, Combined anodic and cathodic hydrogen production from aldehyde oxidation and hydrogen evolution reaction. *Nat. Catal.* **5**, 66–73 (2022).
26. T. W. Kim, K.-S. Choi, Nanoporous $BiVO_4$ photoanodes with dual-layer oxygen evolution catalysts for solar water splitting. *Science* **343**, 990–994 (2014).
27. W. Zhong, R. Sa, L. Li, Y. He, L. Li, J. Bi, Z. Zhuang, Y. Yu, Z. Zou, A covalent organic framework bearing single Ni sites as a synergistic photocatalyst for selective photoreduction of CO_2 to CO. *J. Am. Chem. Soc.* **141**, 7615–7621 (2019).
28. Z. Li, S. Qiu, Y. Song, S. Huang, J. Gao, L. Sun, J. Hou, Engineering single–atom active sites anchored covalent organic frameworks for efficient metallaphotoredox C–N cross–coupling reactions. *Sci. Bull. (Beijing)* **67**, 1971–1981 (2022).
29. A. Jati, K. Dey, M. Nurhuda, M. A. Addicoat, R. Banerjee, B. Maji, Dual metalation in a two-dimensional covalent organic framework for photocatalytic C–N cross–coupling reactions. *J. Am. Chem. Soc.* **144**, 7822–7833 (2022).
30. B. Gao, X. Yu, T. Wang, H. Gong, X. Fan, H. Xue, C. Jiang, K. Chang, X. Huang, J. He, Promoting charge separation by rational integration of a covalent organic framework on a $BiVO_4$ photoanode. *Chem. Commun.* **58**, 1796–1799 (2022).
31. R. T. Gao, L. Wang, Stable cocatalyst-free $BiVO_4$ photoanodes with passivated surface states for photocorrosion inhibition. *Angew. Chem. Int. Ed. Engl.* **59**, 23094–23099 (2020).
32. Y. Xiao, C. Feng, J. Fu, F. Wang, C. Li, V. F. Kunzelmann, C.-M. Jiang, M. Nakabayashi, N. Shibata, I. D. Sharp, K. Domen, Y. Li, Band structure engineering and defect control of Ta_3N_5 for efficient photoelectrochemical water oxidation. *Nat. Catal.* **3**, 932–940 (2020).
33. B. Wu, L. Zhang, B. Jiang, Q. Li, C. Tian, Y. Xie, W. Li, H. Fu, Ultrathin porous carbon nitride bundles with an adjustable energy band structure toward simultaneous solar photocatalytic water splitting and selective phenylcarbinol oxidation. *Angew. Chem. Int. Ed.* **60**, 4815–4822 (2021).
34. H. Li, F. Qin, Z. Yang, X. Cui, J. Wang, L. Zhang, New reaction pathway induced by plasmon for selective benzyl alcohol oxidation on BiOCl possessing oxygen vacancies. *J. Am. Chem. Soc.* **139**, 3513–3521 (2017).
35. X. Sun, X. Luo, X. Zhang, J. Xie, S. Jin, H. Wang, X. Zheng, X. Wu, Y. Xie, Enhanced superoxide generation on defective surfaces for selective photooxidation. *J. Am. Chem. Soc.* **141**, 3797–3801 (2019).
36. F. Xing, R. Zeng, C. Cheng, Q. Liu, C. Huang, POM-incorporated $ZnIn_2S_4$ Z-scheme dual-functional photocatalysts for cooperative benzyl alcohol oxidation and H_2 evolution in aqueous solution. *Appl Catal B: Environ.* **306**, 121087 (2022).
37. Z. Zhou, Y.-N. Xie, W. Zhu, H. Zhao, N. Yang, G. Zhao, Selective photoelectrocatalytic tuning of benzyl alcohol to benzaldehyde for enhanced hydrogen production. *Appl Catal B: Environ.* **286**, 119868 (2021).
38. R. Zhang, M. Shao, Z. Li, F. Ning, M. Wei, D. G. Evans, X. Duan, Photoelectrochemical catalysis toward selective anaerobic oxidation of alcohols. *Chem. A. Eur. J.* **23**, 8142–8147 (2017).
39. Q. Yang, T. Wang, Z. Zheng, B. Xing, C. Li, B. Li, Constructing interfacial active sites in Ru/g-C_3N_{4-x} photocatalyst for boosting H_2 evolution coupled with selective benzyl-alcohol oxidation. *Appl. Catal. B: Environ.* **315**, 121575 (2022).
40. L. Luo, Z.-j. Wang, X. Xiang, D. Yan, J. Ye, Selective activation of benzyl alcohol coupled with photoelectrochemical water oxidation via a radical relay strategy. *ACS Catal.* **10**, 4906–4913 (2020).
41. W. Yang, R. R. Prabhakar, J. Tan, S. D. Tilley, J. Moon, Strategies for enhancing the photocurrent, photovoltage, and stability of photoelectrodes for photoelectrochemical water splitting. *Chem. Soc. Rev.* **48**, 4979–5015 (2019).
42. T. M. Brenner, D. A. Egger, L. Kronik, G. Hodes, D. Cahen, Hybrid organic-inorganic perovskites: Low-cost semiconductors with intriguing charge-transport properties. *Nat. Rev. Mater.* **1**, 15007 (2016).
43. B. Klahr, S. Gimenez, F. Fabregat-Santiago, T. Hamann, J. Bisquert, Water oxidation at hematite photoelectrodes: The role of surface states. *J. Am. Chem. Soc.* **134**, 4294–4302 (2012).
44. B. Klahr, S. Gimenez, F. Fabregat-Santiago, J. Bisquert, T. W. Hamann, Photoelectrochemical and impedance spectroscopic investigation of water oxidation with "Co-Pi"-coated hematite electrodes. *J. Am. Chem. Soc.* **134**, 16693–16700 (2012).
45. Y. Zhang, H. Zhang, A. Liu, C. Chen, W. Song, J. Zhao, Rate-limiting O-O bond formation pathways for water oxidation on hematite photoanode. *J. Am. Chem. Soc.* **140**, 3264–3269 (2018).
46. J. Li, W. Wan, C. A. Triana, H. Chen, Y. Zhao, C. K. Mavrokefalos, G. R. Patzke, Reaction kinetics and interplay of two different surface states on hematite photoanodes for water oxidation. *Nat. Commun.* **12**, 255 (2021).
47. C. A. Mesa, A. Kafizas, L. Francas, S. R. Pendlebury, E. Pastor, Y. Ma, F. Le Formal, M. T. Mayer, M. Gratzel, J. R. Durrant, Kinetics of Photoelectrochemical oxidation of methanol on hematite photoanodes. *J. Am. Chem. Soc.* **139**, 11537–11543 (2017).
48. H. Li, C. Lin, Y. Yang, C. Dong, Y. Min, X. Shi, L. Wang, S. Lu, K. Zhang, Boosting reactive oxygen species generation using inter-facet edge rich WO_3 arrays for photoelectrochemical conversion. *Angew. Chem. Int. Ed. Engl.* **135**, e202210804 (2023).
49. L. Xiong, J. Tang, Strategies and challenges on selectivity of photocatalytic oxidation of organic substances. *Adv. Energy Mater.* **11**, 2003216 (2021).
50. X. Wang, H. Xie, J. G. Knapp, M. C. Wasson, Y. Wu, K. Ma, A. Stone, M. D. Krzyaniak, Y. Chen, X. Zhang, J. M. Notestein, M. R. Wasielewski, O. K. Farha, Mechanistic investigation of enhanced catalytic selectivity toward alcohol oxidation with Ce oxysulfate clusters. *J. Am. Chem. Soc.* **144**, 12092–12101 (2022).
51. Y. Liu, M. Wang, B. Zhang, D. Yan, X. Xiang, Mediating the oxidizing capability of surface-bound hydroxyl radicals produced by photoelectrochemical water oxidation to convert glycerol into dihydroxyacetone. *ACS Catal.* **12**, 6946–6957 (2022).
52. J. Zhang, Y. Nosaka, Photocatalytic oxidation mechanism of methanol and the other reactants in irradiated TiO_2 aqueous suspension investigated by OH radical detection. *Appl. Catal. B: Environ.* **166-167**, 32–36 (2015).
53. Q. Xiang, J. Yu, P. K. Wong, Quantitative characterization of hydroxyl radicals produced by various photocatalysts. *J. Colloid Interface Sci.* **357**, 163–167 (2011).
54. S. Liang, L. Wen, S. Lin, J. Bi, P. Feng, X. Fu, L. Wu, Monolayer HNb_3O_8 for selective photocatalytic oxidation of benzylic alcohols with visible light response. *Angew. Chem. Int. Ed. Engl.* **53**, 2951–2955 (2014).
55. K. Zhang, S. Ravishankar, M. Ma, G. Veerappan, J. Bisquert, F. Fabregat-Santiago, J. H. Park, Overcoming charge collection limitation at solid/liquid interface by a controllable crystal deficient overlayer. *Adv. Energy Mater.* **7**, 1600923 (2017).

Acknowledgments

Funding: This work was supported by the NSFC (T2322013, 22172077, and 22171136), the Natural Science Foundation of Jiangsu Province of China (BK 20211573 and BK 20220079), the Fundamental Research Funds for the Central Universities (30921011216), and the Ministry of Science and ICT through the National Research Foundation of Korea (2022H1D3A3A01077254, RS-00268523, and RS-2023-00302697). J.H.P. acknowledges the support from Yonsei-KIST Convergence Research Program and the Yonsei Lee Youn Jae Fellow Program. **Author contributions:** K.Z. and J.H.P. designed the experiments and revised the manuscript. C.L. carried out the measurements and wrote the manuscript. Z.S. carried out materials synthesis. C. D., Y.L., and W.M. provided experimental assistance. G.Z., B.C., and G.S. provided constructive suggestions for results and provided experimental assistance. **Competing interests:** The authors declare that they have no competing interests. **Data and materials availability:** All data needed to evaluate the conclusions in the paper are present in the paper and/or the Supplementary Materials.

Submitted 27 May 2023
Accepted 5 October 2023
Published 8 November 2023
10.1126/sciadv.adi9442